

Solid-State Nuclear Magnetic Resonance Evidence for an Extended β Strand Conformation of the Membrane-Bound HIV-1 Fusion Peptide[†]

Jun Yang, Charles M. Gabrys, and David P. Weliky*

Department of Chemistry, Michigan State University, East Lansing, Michigan 48824

Received January 4, 2001; Revised Manuscript Received May 4, 2001

ABSTRACT: Solid-state nuclear magnetic resonance (NMR) spectroscopy was applied to the membrane-bound form of a synthetic peptide representing the 23-residue N-terminal fusion peptide domain of the HIV-1 gp41 envelope glycoprotein. 1D solid-state NMR line width measurements of singly ¹³C carbonyl labeled peptides showed that a significant population of the membrane-bound peptide is well-structured in its N-terminal and central regions while the C-terminus has more disorder. There was some dependence of line width on lipid composition, with narrower line widths and hence greater structural order observed for a lipid composition comparable to that found in the virus and its target T cells. In the more ordered N-terminal and central regions of the peptide, the ¹³C carbonyl chemical shifts are consistent with a nonhelical membrane-bound conformation. Additional evidence for a β strand membrane-bound conformation was provided by analysis of 2D rotor-synchronized magic angle spinning NMR spectra of doubly ¹³C carbonyl labeled peptides. Lipid mixing and aqueous contents leakage assays were applied to demonstrate the fusogenicity of the peptide under conditions comparable to those used for the solid-state NMR sample preparation.

Membrane fusion plays an essential role in enveloped virus entry into target host cells (1–3). In some enveloped viruses such as influenza, the virus is first endocytosed. Low pH in the endosome induces fusion between the viral and endosomal membranes and is followed by release of the viral nucleosome into the target cell cytoplasm. In other viruses such as human immunodeficiency virus (HIV),¹ fusion occurs directly between the viral and target cell membranes with subsequent formation of a single membrane enclosing the viral and host cell contents. In this latter case, membrane fusion must be carefully controlled on a spatial and temporal basis so as to keep the host cell intact for viral replication.

Fusion between viruses and host cells (or endosomes) is generally separated into four sequential steps (4): (1) viral/host cell binding; (2) formation of small fusion pores through which electrolytes can pass; (3) mixing of viral and host cell lipids; (4) formation of a large fusion pore through which larger molecules can pass and creation of a single virus/host cell moiety. For the influenza and HIV viruses, fusion is mediated by conformational changes in the viral envelope proteins attached to the viral membrane (5–8). For both viruses, these conformational changes are believed to lead to exposure of a hydrophobic region at the N-terminus of one of the envelope proteins (9, 10). This ~20 amino acid region has been named the ‘fusion peptide’ because mutations or deletions in this region greatly disrupt viral/host cell membrane fusion and infection (11–14). Additionally, radioactive labeling has demonstrated that the fusion peptide is the only region of the influenza viral fusion proteins which inserts deeply into membranes during fusion (15).

The significance of the fusion peptide is also suggested from atomic-resolution structures of envelope protein domains. Such structures exist for large parts of the influenza hemagglutinin fusion proteins both at nonfusogenic pH 7 (5) and at fusogenic pH 5 (6, 16), although the fusion peptide domain was deleted from the constructs used in the latter structures. These structures provide evidence for a major influenza envelope protein conformational change under fusogenic conditions which moves the fusion peptide by ~100 Å relative to the rest of the molecule (17). Analysis of these structures and consideration of other fusion data have led to at least four proposed models of influenza/endosome fusion (4, 6, 17–19). In all of these models, membrane insertion of the fusion peptide and the accompanying bilayer disruption play an integral role in membrane fusion.

[†] This work was supported in part by a Camille and Henry Dreyfus Foundation New Faculty Award and by NIH Award R21-AI47153 to D.P.W.

* To whom correspondence should be addressed. Telephone: 517-355-9715. Fax: 517-353-1793. E-mail: weliky@cem.msu.edu.

¹ Abbreviations: ANTS, 8-aminonaphthalene-1,3,6-trisulfonic acid; CD, circular dichroism; CP, cross-polarization; CS, chemical shift; CSA, chemical shift anisotropy; DMPC, dimyristoyl-*sn*-glycero-3-phosphocholine; DMPS, dimyristoyl-*sn*-glycero-3-[phospho-L-serine]; DPX, *p*-xylene-bispyridinium bromide; DTPC, di-*o*-tetradecyl-*sn*-glycero-3-phosphocholine; ESR, electron spin resonance; FMOC, 9-fluorenylmethoxycarbonyl; FP, fusion peptide; fwhm, full-width-at-half-maximum; HEPES, *N*-(2-hydroxyethyl)piperazine-*N'*-2-ethanesulfonic acid; HIV, human immunodeficiency virus; HPLC, high-performance liquid chromatography; LM, lipid mixture; LUV, large unilamellar vesicles; MAS, magic angle spinning; NMR, nuclear magnetic resonance; *N*-NBD-PE, *N*-(7-nitro-2,1,3-benzoxadiazol-4-yl)phosphatidylethanolamine; *N*-Rh-PE, *N*-(lissamine Rhodamine B sulfonyl)phosphatidylethanolamine; PBS, phosphate-buffered saline; PI, phosphatidylinositol; POPC, 1-palmitoyl-2-oleoyl-*sn*-glycero-3-phosphocholine; POPE, 1-palmitoyl-2-oleoyl-*sn*-glycero-3-phosphoethanolamine; POPG, 1-palmitoyl-2-oleoyl-*sn*-glycero-3-[phospho-*rac*-(1-glycerol)]; POPS, 1-palmitoyl-2-oleoyl-*sn*-glycero-3-[phospho-L-serine]; RET, resonance energy transfer; SDS, sodium dodecyl sulfate; SIV, simian immunodeficiency virus; TFA, trifluoroacetic acid; 1D, one-dimensional; 2D, two-dimensional.

For HIV, fusion and infection are mediated by the heavily glycosylated, predominantly extraviral envelope proteins gp120 and gp41 which form a noncovalently bound complex. The complex is attached to the virus through a transmembrane segment in gp41, and the fusion peptide domain is located at the N-terminus of the gp41 extraviral ectodomain. In vivo fusion is initiated by tight binding of gp120 to the CD4 and chemokine receptors of target human T or macrophage cells (2). This interaction is followed by a series of poorly understood conformational changes and intermediates which are believed to eventually lead to exposure of the fusion peptide and subsequent viral/host cell membrane fusion (8, 20).

Recent atomic-resolution structural data on HIV-1 viral envelope protein domains have given insight into its fusion pathways. In 1998, a crystal structure was published for a deglycosylated core of HIV-1 gp120 bound to a CD4 domain and a neutralizing antibody (7). Structures have also been published for part of the ectodomain of gp41 (20–25). In these structures, the ectodomain of an individual gp41 molecule folds back on itself, and the molecules associate as very stable coiled coil trimers ($T_m = 93$ °C) (26). The inferred proximity of the gp41 transmembrane and fusion peptide domains suggests that gp41 may catalyze membrane fusion by bringing the viral and host cell membranes close together (20).

The gp41 trimeric coiled coil motif was also observed in the structure of the low-pH influenza hemagglutinin protein as well as in recent structures of envelope proteins of leukemia retroviruses (27, 28), paramyxoviruses (29), and ebola virus (30, 31). This shared motif suggests that the mechanism of membrane fusion may be similar in all of these viruses. Fusion may also require oligomers of envelope protein trimers, as has been suggested in recent modeling studies of influenza and HIV-1-mediated fusion (32, 33).

Despite its biological importance in fusion, the fusion peptide domain has not been included any of the gp41 constructs used for high-resolution structural analysis, or indeed in any fusogenic protein high-resolution structure. The hydrophobicity of the fusion peptide impairs the high protein aqueous solubility required for crystallographic and solution NMR techniques, and neither technique is well-suited to studies in intact membrane systems.

Solid-state NMR is suited to atomic-resolution structural measurements on proteins in intact membranes because unlike X-ray techniques, crystals are not required, and unlike solution NMR, high (>30 000) molecular weight systems can be routinely studied (34, 35). Systems recently studied with solid-state NMR techniques include the membrane-bound channels gramicidin (36) and colicin (37), β -amyloid fibrils implicated in Alzheimer's disease (38, 39), the *E. coli* serine receptor (40), the enzymes triosephosphate isomerase (41) and EPSP synthase (42, 43), and a HIV-1 peptide/neutralizing antibody complex (44).

In our solid-state NMR studies, we have used peptides composed of the ~20-residue N-terminal fusion peptide domain of the gp41 envelope protein. Significantly, there is strong experimental evidence that structural and motional studies of membrane-bound fusion peptides provide important information about intact envelope protein insertion into target membranes and the consequent bilayer disruption and fusion. The bases for this assertion are: (1) the free fusion

peptide causes fusion of liposomes and erythrocytes; and (2) numerous mutational studies have shown strong correlations between fusion peptide-induced liposome fusion and viral/host cell fusion (10, 45–55).

Although there are strong similarities between fusion peptide-induced fusion and HIV-1/host cell fusion, one difference between them is that the fusion peptide is initially free in solution whereas the gp41 fusion protein is always attached through a transmembrane segment to the virus. In influenza viral fusion, there is evidence that the transmembrane domain is not required for the lipid mixing step but is required for formation of a fusion pore (56). However, for HIV-1 fusion peptide-induced fusion of liposomes, a fusion pore has been indirectly detected through observation of aqueous contents mixing between liposomes (54). For both HIV-1 fusion peptide-induced liposome fusion and influenza viral fusion, there is also significant leakage of aqueous contents (51, 57).

Our solid-state NMR measurements were made on a consensus 23-residue HIV-1 fusion peptide sequence, H-Ala-Val-Gly-Ile-Gly-Ala-Leu-Phe-Leu-Gly-Phe-Leu-Gly-Ala-Ala-Gly-Ser-Thr-Met-Gly-Ala-Arg-Ser-NH₂. For comparison, a consensus sequence of the more polar influenza A fusion peptide is: Gly-Leu-Phe-Gly-Ala-Ile-Ala-Gly-Phe-Ile-Glu-Asn-Gly-Trp-Glu-Gly-Met-Ile-Asp-Gly-Trp-Tyr-Gly. For the influenza fusion peptide, infrared, circular dichroism (CD), and electron spin resonance (ESR) data are most consistent with a 'tilted helix' structural model for fusion peptide interaction with the membrane (10, 58). In this model, the peptide helix makes an oblique angle with respect to the membrane bilayer normal (59). The ESR studies also suggest that at 1:1000 peptide:lipid mole ratios, the influenza peptide is monomeric in the membrane (58).

By contrast, previous CD, infrared, solution NMR, fluorescence, and ESR studies have yielded complex and sometimes contradictory results on the membrane-bound structure of the HIV-1 fusion peptide domain. CD measurements on the HIV-1 fusion peptide show significant helical character for samples in organic solvent (52, 60–63), in sodium dodecyl sulfate (SDS) detergent at a 1:200 peptide:lipid ratio (52, 61, 64), and in an environment of negatively charged POPG vesicles with a 1:200 peptide:lipid mole ratio (46). NMR studies on the peptide in SDS micelles are also consistent with a helical central region (62). By contrast, at 1:10 peptide:SDS molar ratio (61) or 1:30 peptide:POPG mole ratio (46), there is significant β strand character. Similar results were found in 1:1 mixtures of neutral/negatively charged lipids (65).

With neutral lipid vesicles or erythrocyte ghosts at peptide:lipid ratios of ~1:200, there are two infrared reports of predominantly helical structure (51, 61), three reports of predominantly β structure (46, 53, 66), and one report of mixed helical and β structure (48). Two investigators report that the peptide conformation changes from helical to β as the peptide:lipid mole ratio is increased from 1:200 to 1:30 (51, 61) while two others report that the β conformation does not change with these ratios (46, 53). These differences in structure may have to do with differences in peptide sequence, lipid composition, sample preparation, or hydration level. A recent infrared study of the peptide in a neutral membrane monolayer was also consistent with a β structure (67).

Fluorescence and ESR measurements on derivatized HIV-1 fusion peptides in membrane vesicle environments provide evidence that the N-terminal and central regions are inserted into the membrane and the C-terminus is outside the membrane (52, 61). In some contrast, a H/D NMR exchange study in SDS micelles suggests that the N-terminus is outside the micelle (68).

Fluorescence resonance energy transfer measurements are consistent with peptide oligomerization in the membrane-bound state for peptide:lipid ratio greater than 1:5000 (52). In some contrast, ESR data indicate highly mobile monomeric peptide at peptide:lipid ratios $\leq 1:1000$ and oligomeric peptide at peptide:lipid ratios $\geq 1:800$ (61).

Our solid-state NMR studies strongly suggest that the membrane-bound HIV-1 fusion peptide forms a predominant β strand conformation in its N-terminal and central regions and is more disordered at the C-terminus. The β strand conformation would be consistent with a hairpin structure and/or with a parallel or antiparallel oligomeric sheet.

MATERIALS AND METHODS

Materials. Rink amide resin was purchased from Advanced Chemtech (Louisville, KY), and 9-fluorenylmethoxycarbonyl (Fmoc)-amino acids were obtained from Peptides International (Louisville, KY). ^{13}C carbonyl labeled amino acids were purchased from Icon Services Inc. (Summit, NJ), and the Fmoc group was added using literature methods (69, 70). Di-*o*-tetradecyl-*sn*-glycero-3-phosphocholine (DTPC), dimyristoyl-*sn*-glycero-3-phosphocholine (DMPC), dimyristoyl-*sn*-glycero-3-[phospho-L-serine] (DMPS), 1-palmitoyl-2-oleoyl-*sn*-glycero-3-[phospho-*rac*-(1-glycerol)] (POPG), 1-palmitoyl-2-oleoyl-*sn*-glycero-3-phosphocholine (POPC), 1-palmitoyl-2-oleoyl-*sn*-glycero-3-phosphoethanolamine (POPE), 1-palmitoyl-2-oleoyl-*sn*-glycero-3-[phospho-L-serine] (POPS), phosphatidylinositol (PI), sphingomyelin, *N*-(7-nitro-2,1,3-benzoxadiazol-4-yl)phosphatidylethanolamine (*N*-NBD-PE), *N*-(lissamine Rhodamine B sulfonyl)phosphatidylethanolamine (*N*-Rh-PE), and cholesterol were purchased from Avanti Polar Lipids, Inc. (Alabaster, AL). ANTS (8-aminonaphthalene-1,3,6-trisulfonic acid) and DPX (*p*-xylene-bispyridinium bromide) were purchased from Molecular Probes (Eugene, OR). The Micro BCA protein assay was obtained from Pierce (Rockford, IL). *N*-(2-Hydroxyethyl)-piperazine-*N'*-2-ethanesulfonic acid (HEPES) and Triton X-100 were obtained from Sigma. All other reagents were analytical grade.

Peptides. FP23 peptides corresponding to the 23 N-terminal residues (AVGIGALFLGFLGAAGSTMGARS) of the LAV_{1a} strain of HIV-1 gp41 were synthesized as their C-terminal amides using a peptide synthesizer (ABI 431A, Foster City, CA) equipped for Fmoc chemistry. All amino acids were single-coupled using 2 h coupling times. Unlabeled, singly ^{13}C carbonyl labeled, and doubly ^{13}C carbonyl labeled peptides were synthesized. The singly ^{13}C labeled peptides are denoted FP23-V2, FP23-F8, FP23-F11, FP23-A15, and FP23-A21, and the doubly labeled peptides are denoted FP23-A1V2, FP23-L7F8, FP23-G10F11, and FP23-A14A15. Peptides were cleaved from the resin in a 3 h reaction using a mixture of TFA/H₂O/phenol/thioanisole/ethanedithiol in a 33:2:2:2:1 volume ratio. Peptides were subsequently purified by reversed-phase HPLC using a

preparative C₁₈ column (Vydac, Hesperia, CA) and a water/acetonitrile gradient containing 0.1% TFA. The peptide eluted at $\sim 60\%$ acetonitrile concentration. Mass spectroscopy was used to verify peptide purity. The overall purified yield was $\sim 25\%$.

Lipid Preparation. Samples were prepared either using single lipids or using lipid/cholesterol mixtures reflecting the approximate lipid and cholesterol content of the HIV-1 virus and its target T-cells (71). Three such mixtures were used: (a) "LM-1" had POPC, POPE, DMPS, and cholesterol in a 10:6:4:10 ratio; (b) "LM-2" had POPC, POPE, DMPS, sphingomyelin, and cholesterol in a 10:6:4:2:10 ratio; (c) "LM-3" had POPC, POPE, POPS, sphingomyelin, PI, and cholesterol in a 10:5:2:2:1:10 mole ratio. Lipid and cholesterol powders were dissolved together in chloroform. The chloroform was removed under a stream of nitrogen followed by overnight vacuum-pumping. Lipid dispersions were formed by addition of water or buffer containing 0.01% Na₂S₂O₈ followed by homogenization with 10 freeze-thaw cycles. Large unilamellar vesicles (LUV) of 100 nm diameter were prepared by extrusion (72). In this approach, lipid dispersions were extruded ~ 30 times through two stacked 0.1 μm polycarbonate filters (Avestin, Inc., Ottawa, ON, Canada).

Peptide Aggregation. Peptide aggregation in solution was estimated from measurements of peptide concentration (by the BCA assay) in solution before and after centrifugation. Centrifugation was done either on a Sorvall RC-5B centrifuge (Newtown, CT) with a GSA rotor (14000g, 90 min) or on a Sorvall Ultra 80 ultracentrifuge (Newtown, CT) with a SW50.1 or SW25.1 rotor (100000–150000g, 120–240 min).

Lipid Mixing Assay for Membrane Fusion. The resonance energy transfer (RET) assay of Struck et al. was used to monitor membrane fusion (73). Two types of 100 nm diameter LM-3 LUV were prepared. One set contained 2 mol % of the fluorescent lipid *N*-NBD-PE and 2 mol % of the quenching lipid *N*-Rh-PE while the other set only contained unlabeled lipids. Fluorescently labeled and unlabeled vesicles were mixed in a 1:9 ratio. Following addition of FP23, lipid mixing between labeled and unlabeled vesicles caused dilution of the labeled lipids with a resulting increase of fluorescence. Fluorescence was recorded using 4 nm bandwidth on an Instruments S. A. Fluoromax-2 (Edison, NJ) spectrofluorometer operating at excitation and emission wavelengths of 465 and 530 nm, respectively. A siliconized glass cuvette was used with continuous stirring in a thermostated cuvette holder. Measurements were carried out at 37 °C with 2 mL of 150 μM LUV in 5 mM HEPES (pH 7.0). A small quantity of aqueous 1 mM FP23 peptide solution was added to achieve the desired peptide:lipid mole ratio, and the change in fluorescence of the sample was monitored following this addition. The initial residual fluorescence intensity, F_0 , referenced zero lipid mixing. The maximum fluorescence intensity, F_{max} , was obtained following addition of 20 μL of 10% Triton X-100. Percent lipid mixing at time t was given by $[(F_t - F_0)/(F_{\text{max}} - F_0)] \times 100$.

Leakage Studies. Aqueous content leakage from liposomes was monitored by the ANTS/DPX assay (74). The 100 nm diameter LM-3 LUV were prepared in 5 mM HEPES (pH 7.0) solution which also contained the fluorescent molecule ANTS and the quenching molecule DPX at 12.5 and 45 mM,

respectively. ANTS and DPX were then removed from the extravesicular medium by dialysis against 65 mM HEPES solution. After addition of a small quantity of 1 mM aqueous peptide solution, vesicle leakage was monitored by the increase in ANTS fluorescence. Fluorescence measurements were performed at excitation and emission wavelengths of 355 and 520 nm, respectively. Measurements were made at 37 °C using 2 mL of 80 μ M LUV in 65 mM HEPES (pH 7.0). Percent leakage was defined in the same way as was used for the lipid mixing assay.

Solid-State NMR Sample Preparation. Samples were typically prepared using 0.01% NaN₃ in either unbuffered water or 5 mM HEPES buffer (pH 7.0). Samples were prepared by two different methods. Method (1): Mixtures of peptide (15–150 μ M) and lipid dispersion or vesicles (1–30 mM) in 4 or 30 mL total volume were kept at room temperature overnight to ensure maximum peptide/lipid binding. Subsequent centrifugation of the peptide/lipid complex, typically at 100000–150000g for 2–4 h, pelleted down the complex and left unbound peptide in the supernatant. The peptide/lipid pellet formed after ultracentrifugation was transferred by spatula to a 220 μ L magic angle spinning (MAS) NMR rotor. Method (2): Mixtures of peptide (1–10 mM) and lipid dispersion (200–400 mM) were mixed to form \sim 200 μ L total volume. The mixtures were transferred directly to the MAS rotor. The main differences between methods (1) and (2) were: (a) unbound peptide was separated from bound peptide for method (1) but not for method (2); and (b) 10–100-fold lower peptide and lipid concentrations were used for method (1) compared to method (2). As described under Results, these differences are not significant because: (a) the peptide binds strongly to lipid; and (b) the experimental solid-state NMR spectra are similar over a large range of initial peptide concentrations.

Measurement of Peptide/Lipid Binding. For solid-state NMR preparation method (1), peptide/lipid binding was determined through BCA assay measurement of the peptide concentration in the solution prior to addition of lipid and after ultracentrifugation. Under ultracentrifugation, all lipid was pelleted and there was no interference from unpelleted lipid in the BCA assay. Controls were run with peptide-only samples to ensure that the peptide did not pellet by itself.

For solid-state NMR preparation method (2), \sim 800 μ L of water was added to the peptide/lipid dispersion, the sample was vortexed, and the peptide/lipid mixtures were spun down at 10000–14000g. The unbound peptide concentration in the supernatant was measured by the BCA assay. Under these centrifugation conditions, all of the lipid was pelleted, and there was no interference from unpelleted lipid in the BCA assay.

One-Dimensional (1D) Solid-State NMR Experiments. Measurements were made on a 9.4 T spectrometer (Varian VXR, Palo Alto, CA) using a double resonance MAS probe equipped with 7 mm diameter rotors. The NMR detection channel was tuned to ¹³C at 100.6 MHz, and the decoupling channel was tuned to ¹H at 400.0 MHz. Experiments were carried out using a spinning frequency between 3.5 and 4.0 kHz. Application of 1 ms of cross-polarization (CP) at 47 kHz was followed by signal detection with decoupling at 75 kHz. The recycle delay was 0.5 s. For typical samples containing \sim 0.5 μ mol of labeled peptide, a single spectrum

was the average of 80 000–160 000 scans. All chemical shifts were externally referenced to the methylene carbon resonance of adamantane (38.2 ppm). Spectra were processed with 25 Hz line broadening. Strong ¹³C signals could not be observed above –20 °C, presumably because of signal attenuation due to slow motion. Hence, samples were cooled to –50 °C either slowly in the NMR probe or by fast freezing in liquid nitrogen. Both freezing techniques gave comparable spectra.

In most cases, the samples contained one or two ¹³C peptide carbonyl backbone labels, and the NMR signals from these labeled sites were of greatest interest. The labeled site signals were often unresolved from large natural-abundance signals from lipid carbonyls and from unlabeled peptide carbonyls. To uniquely observe the labeled site signals, spectra were also taken of unlabeled peptide/lipid samples. Subtraction of the natural-abundance spectra from the labeled spectra yielded a difference spectrum of the labeled site(s). To uniquely observe carbonyl signals from Ala-1, Gly-10, and Ala-14, for which singly labeled FP23 peptides had not been synthesized, difference spectra were taken between samples made with FP23-A1V2, FP23-G10F11, and FP23-A14A15 and samples made with FP23-V2, FP23-F11, and FP23-A15, respectively. For most samples, subtraction was considered to be optimal when large lipid aliphatic signals at \sim 35 ppm were minimized in the difference spectrum. In a difference spectrum, the labeled carbonyl peak chemical shift and spectral line shape were fairly insensitive to the goodness of subtraction in the aliphatic region, which gave an uncertainty of \sim \pm 0.2 ppm in both shift and fwhm line width.

Two-Dimensional (2D) Experiments. 2D exchange spectra were obtained at 2.5 kHz spinning frequency and –50 °C on doubly labeled peptide/lipid samples. Spectra were acquired using the rotor-synchronized pulse sequence (CP)– t_1 –($\pi/2$)– τ –($\pi/2$)– t_2 , in which (CP) represents cross-polarization from ¹H to ¹³C, t_1 is the evolution period, $\pi/2$ represents a ¹³C pulse, τ (500 ms) is the spin diffusion period, and t_2 is the ¹³C detection period (75, 76). Samples typically contained 2 μ mol of labeled peptide. The experiment was run under the following conditions: (1) 800 μ s CP was made with ¹³C RF radiation at 47 kHz and a linear ramp on ¹H between 42 and 52 kHz; (2) 47 kHz ¹³C $\pi/2$ pulses were applied; (3) 72 t_1 points were taken with an increment of 40 μ s; (4) signals were acquired for 10 ms during t_2 ; (5) decoupling at 75 kHz was applied during t_1 and t_2 but not during τ ; and (6) the recycle delay was 0.5 s. Complete data sets were collected in 12 h blocks and then summed together, with 10–15 blocks in a final data set.

Spectra were processed using nmrPipe software (77) with 150 Hz line broadening in the t_1 and the t_2 dimensions. In the 2D spectrum, structural information is contained in the relative intensities of the off-diagonal cross-peaks between the spinning sidebands of the labeled carbonyl sites. These intensities depend on the relative orientations of the two labeled carbonyls' chemical shift anisotropy (CSA) tensors and can be directly related to the dihedral angles ϕ and ψ of the more C-terminal labeled residue (75, 76).

Integrated experimental cross-peak intensities were calculated by summing the intensities of points in a 1 ppm \times 1 ppm area. To determine the most likely values for ϕ and ψ , experimental cross-peak intensities were compared to

simulated cross-peak intensities calculated for a grid of ϕ and ψ values. This grid was made in 5° increments for $-180^\circ \leq \phi \leq 0^\circ$ and $-180^\circ \leq \psi \leq 180^\circ$. The simulated cross-peak intensities were calculated from a computer program supplied by R. Tycko (NIH) and included a small contribution (<20%) from longitudinal ^{14}N relaxation, whose characteristic time is shorter than the 500 ms exchange time. The simulated cross-peak intensity pattern for a (ϕ, ψ) pair is the same as that for $(-\phi, -\psi)$. In addition to their dependence on ϕ and ψ , the simulated intensities depend on the orientation of the carbonyl CSA principal axes relative to the peptide group and on the carbonyl CSA principal values. The former were taken from the literature (78) while the latter were experimentally determined from measurements of the 1D peak spinning sideband intensities measured at a few different spinning frequencies between 2 and 4 kHz (79). In the FP23-L7F8/DTPC sample, the sideband intensities were measured from raw 1D spectra and contained a small contribution (<10%) from natural-abundance signals of unlabeled peptide carbonyls. For the LM-3 samples, the sideband intensities were measured from 1D difference spectra and only contained contributions from the labeled carbonyl nuclei. In all samples, the chemical shifts of the two labeled carbonyl nuclei were not resolved, so the same set of principal values was assumed for both nuclei.

In the 2D analysis, the total squared deviation $\chi^2(\phi, \psi)$ between experiment and simulation was evaluated as

$$\chi^2(\phi, \psi) = \sum_i [E_i - \lambda(\phi, \psi)S_i(\phi, \psi)]^2 / \sigma^2, \quad i = 1-N \quad (1)$$

where E_i and $S_i(\phi, \psi)$ are experimental and simulated off-diagonal cross-peak intensities, σ^2 is the mean-squared noise per data point, $\lambda(\phi, \psi)$ is a scaling factor calculated to minimize χ^2 at each (ϕ, ψ) pair, and N is the total number of data points. Because mirror image (across-the-diagonal) cross-peaks always have the same simulated intensity, the experimental mirror image cross-peak intensities were summed, and the 20 off-diagonal cross-peak intensities (from a 5×5 2D spectral array of spinning sidebands) were reduced to 10 data points.

RESULTS

Peptide Aggregation in Aqueous Solution. NMR of FP23 has also been done in aqueous solution at pH 3.3 and would only be possible if the peptide were monomeric or formed small oligomers (62). Contrarily, in pH 7.4 PBS (phosphate-buffered saline), electron microscopy has revealed formation of fibrillar fusion peptide aggregates (53, 60). With solid-state NMR sample preparation method (1), centrifugation is used to pellet membrane-bound peptide and could also pellet large aggregates of unbound peptide. To find nonaggregating conditions, a systematic investigation was carried out on peptide pelleting in the absence of membrane.

Results from these studies are presented in Table 1, with uncertainties of $\pm 10\%$ in the peptide concentration measurements. In unbuffered solution, the fusion peptide formed a clear solution, even at 10 mM concentrations. After addition of phosphate buffer or NaCl, the solution became cloudy. Formation of large aggregates was confirmed by peptide pelleting after centrifugation. Large aggregates were not formed in 100 mM acetate buffer, pH 4.5, or in 5 mM HEPES buffer, pH 7.0. Thus, there appear to be pH and ionic

Table 1: FP23 Aggregation in Solution

initial peptide concn (μM)	solution conditions	% soluble peptide ^{a,b}
6200	unbuffered H_2O	90
1100	5 mM HEPES, pH 7.0, sitting for 2 days	80
15	5 mM HEPES, pH 7.0, sitting for 1 day	>90
210	100 mM acetate, pH 4.5	>90
190	10 mM phosphate, pH 7.0	2
1100	5 mM HEPES, pH 7.0, 20 mM NaCl	18

^a Rows 1, 2, 4–6 ($\geq 190 \mu\text{M}$ peptide): concentration measured after centrifugation at 14000g for 90 min. Row 3 (15 μM peptide): concentration measured after centrifugation at 100000g for 120 min.

^b Estimated error: $\pm 10\%$.

strength effects on aggregation. The differences in aggregation between HEPES and phosphate or NaCl may be a result of the differences in their molecular sizes. Based on these results, most solid-state NMR samples were made using 15–150 μM peptide concentration in 5 mM pH 7.0 HEPES buffer, which is close to the physiological pH of 7.4 for HIV-1/host cell fusion. Although physiological solution contains ~ 140 mM NaCl, it was omitted from the sample preparation because of its effects on aggregation. It would be possible to add NaCl after the peptide has bound to the membrane.

The oligomerization of viral envelope proteins is well-known, and there is some evidence that fusion peptide oligomerization is a structural requirement for membrane fusion (52). Fusion peptide oligomers might be preformed in solution and bind as a unit to the membrane, or oligomers might only form during interaction with the membrane. Under proper conditions, our ultracentrifugation data demonstrate that large peptide aggregates are not formed in solution. To probe the possible presence and size of smaller solution-phase oligomers, further analysis was carried out on ultracentrifugation and solution NMR data.

Table 1 demonstrates that at 15 μM peptide concentration in 5 mM pH 7.0 HEPES, ultracentrifugation gave negligible precipitation of peptide. With a simplified model for ultracentrifugation, these data have been used to estimate the maximum size of any peptide aggregate (80). First, an upper limit is estimated for the sedimentation coefficient using the assumption that peptide pelleting requires the peptide concentration boundary to move from the top of the tube to the bottom of the tube during centrifugation. This assumption is translated into an inequality in the standard formula for the sedimentation coefficient S :

$$S < (1/\omega^2) \times \ln(x_b/x_t)/t_c \quad (2)$$

where ω is the angular centrifugation velocity, x_b is the radial position of the bottom of the centrifuge tube, x_t is the radial position of the top of the centrifuge tube, and t_c is the centrifugation time. Using the experimental parameters of $\omega = 4200 \text{ s}^{-1}$, $x_b = 10.7 \text{ cm}$, $x_t = 7.3 \text{ cm}$, and $t_c = 15000 \text{ s}$, an upper limit of $\sim 1.5 \times 10^{-12} \text{ s}$ is placed on S . Using a standard formula, this limit can be related to an upper limit on the mass M of any aggregates:

$$S = M \times (1 - V_2\rho)/N_0f \quad (3)$$

where V_2 is the specific volume of protein, ρ is the density of water, N_0 is Avogadro's number, and f is the frictional coefficient. A Stokes' Law approximation is used to estimate

Table 2: FP23 Binding to Membranes

lipid	peptide (mM): lipid (mM) ^a ratio	% binding ^b
DTPC	0.50:100	75
DMPC	0.50:100	80
POPG	0.50:100	90
DTPC	0.10:10	80
LM-2	0.10:10	95
LM-1	0.12:25	99
LM-3	0.012:1	97
LM-3 ^c	0.012:1	96

^a The samples for the first three rows were made by preparation method (2), and the samples for the next five rows were made by preparation method (1). ^b Estimated error: $\pm 10\%$. ^c Measurements were made with lipid dispersion samples except for this entry which was made with 100 nm diameter vesicles.

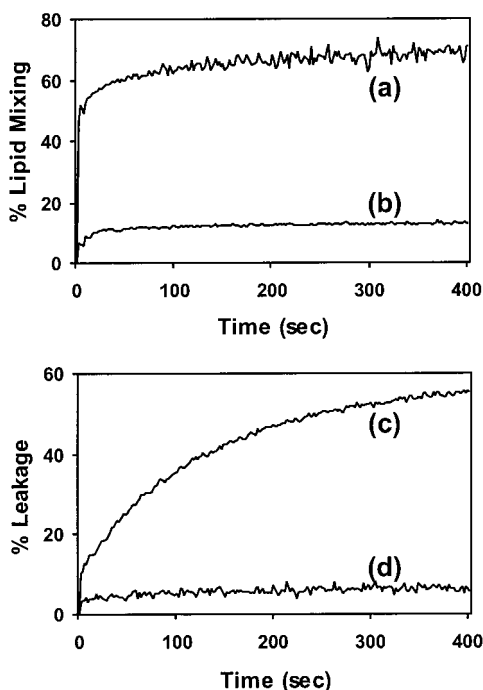


FIGURE 1: FP23-induced lipid mixing (top) and FP23-promoted aqueous contents leakage (bottom) as observed by fluorescence assays at 37 °C. For the lipid mixing assay, 150 μM LM-3 lipid was extruded into 100 nm diameter vesicles. Lipid mixing was induced with (a) 7.5 μM and (b) 1.5 μM FP23. For the aqueous contents leakage assay, 80 μM LM-3 lipid was extruded into 100 nm diameter vesicles loaded with ANTS/DPX. Leakage was promoted by FP23 at (c) 4 μM and (d) 1 μM concentrations.

f and includes a shape factor of 4 for the putative fibrillar shape of any aggregates:

$$f \sim 24\pi\eta(3MV_2/4\pi N_0)^{1/3} \quad (4)$$

where η is the viscosity of water. A combination of eqs 3 and 4 with values for V_2 , $V_2\rho$, and η of 0.7 cm^3/g , 0.7, and 10^{-2} $\text{g}/(\text{cm}\cdot\text{s})$, respectively, provides an upper limit of ~ 900 FP23 molecules in any aggregate.

Solution NMR line widths also gave some information about aggregate size. At all pHs, there is a molecular tumbling contribution to the observed line width which is proportional to molecular weight (81). For 100 μM FP23 solutions at pH 4 and 7, the observed 600 MHz amide ^1H solution NMR line widths were 4 and 15 Hz, respectively, which can be approximately correlated with the masses of

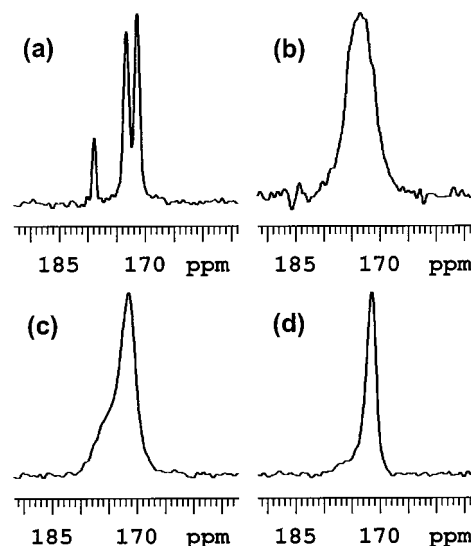


FIGURE 2: ^{13}C solid-state NMR CP/MAS spectra of (a) polycrystalline Ala-Gly-Gly composed of 95% natural-abundance peptide and 5% Ala-1, Gly-2 doubly ^{13}C carbonyl labeled peptide; (b) 20 mM frozen aqueous solution of HGRVGIYFGMK epitope peptide which was ^{13}C carbonyl labeled at Phe-8; (c) 7.5 mM frozen aqueous solution of FP23-L7F8; and (d) FP23-L7F8/DTPC made by preparation method (2) at a 1:20 peptide:lipid mole ratio. The AGG spectrum was taken at room temperature, and the other spectra were taken at -50 °C.

FP23 monomers and heptamers, respectively (81). The derivation of these masses is based on a tumbling model of a spherical protein with a single hydration shell. At pH 7, solvent exchange also contributes to the observed line width, so the derived heptamer mass may be an overestimate.

Peptide Binding to Lipids. As delineated in Table 2, there is strong binding between fusion peptide and membrane bilayers under solid-state NMR sample preparation conditions. Binding to LM is quantitative, and binding to pure neutral or negatively charged lipids is 75–90%.

FP23-Induced Fusion of LM Vesicles. To test whether FP23 is fusogenic under conditions comparable to those used for solid-state NMR sample preparation, measurements were made on FP23-induced lipid mixing between vesicles and aqueous contents leakage from vesicles. Figure 1 demonstrates both effects and gives results comparable to those obtained by other investigators (53, 66). At low peptide:lipid mole ratio ($\leq 1:80$), lipid mixing and leakage only proceed to $\sim 10\%$ of their maximal values. At a peptide:lipid ratio of 1:20, fusion and leakage are much more efficient, which suggests that a vesicle's fusogenicity is related to the number of incorporated FP23 molecules. At 1:100 peptide:lipid mole ratio, the final extent of percent lipid mixing is much less than the 45% which would be observed if each vesicle fused with one other vesicle (82). Therefore, it appears that not all vesicles fuse at lower peptide:lipid ratios. This result is interesting because even at 1:100 peptide:lipid ratio with maximal binding, there are on average 10^2 – 10^3 peptide molecules per 100 nm diameter vesicle. The leakage rates of FP23 contrast with those of model helical peptides such as GALA which induce significant leakage at much lower peptide:lipid ratios ($\sim 1:5000$) (83). GALA lipid mixing rates are comparable to those of FP23 (82).

Dependence of 1D NMR Spectra on Sample Conditions. Figure 2 displays the 1D MAS spectra of different ^{13}C

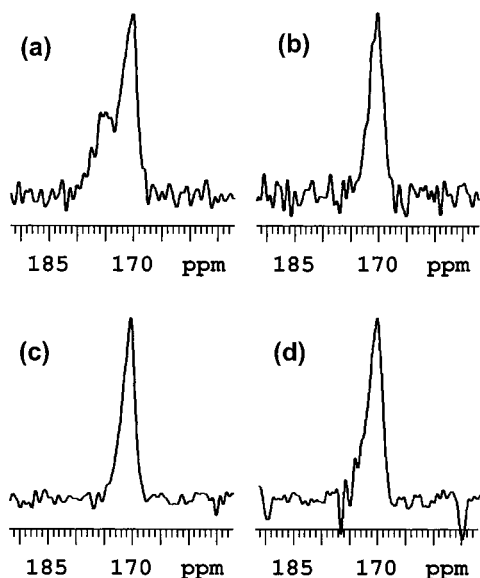


FIGURE 3: ^{13}C solid-state NMR spectra of samples made from FP23-F8 bound to (a) DTPC dispersion, (b) LM-1 dispersion, (c) LM-3 dispersion, and (d) 100 nm diameter LM-3 vesicles. Samples were prepared by method (1) with a peptide:lipid mole ratio of (a and b) 1:200 and (c and d) 1:80. Spectra were taken at -50°C using CP/MAS and 75 kHz ^1H decoupling. (a) is a raw spectrum, (b) is a difference spectrum between a FP23-F8/LM-1 and a LM-1 sample, and (c) and (d) are difference spectra between FP23-F8/LM-3 and unlabeled FP23/LM-3 samples.

carbonyl labeled peptides. Generally, the carbonyl line width is a marker of the structural heterogeneity in the vicinity of the labeled nucleus or nuclei. For example, Figure 2(a) displays the spectrum of polycrystalline Ala-Gly-Gly while Figure 2(b) displays the spectrum for an unstructured singly ^{13}C carbonyl labeled epitope peptide, HGRVGIYFGMK, in frozen solution. The observed full-width-at-half-maximum (fwhm) line widths of ~ 1 and ~ 6 ppm mark the two extrema of highly structured and unstructured residues, respectively.

Figure 2(c) and Figure 2(d) respectively display the 1D spectra of FP23-L7F8 in 7.5 mM frozen solution and hydrated lipid DTPC environments (1:20 peptide:lipid mole ratio). The lipid sample in (d) was prepared by method (2) using 100 μL of the (c) solution. DTPC was initially chosen for these studies because it is ether-linked rather than ester-linked and hence has no natural-abundance carbonyl background. Thus, in (c) and (d), the labeled carbonyl carbons contributed 90% of the observed intensity. The signals from the two labeled carbonyls were unresolved. In the presence of DTPC, the line width is ~ 2 ppm fwhm and is narrower than that found in frozen solution. These data indicate that: (1) the L7F8 region of FP23 interacts with lipid; and (2) in the presence of lipid, the L7F8 region is reasonably well-structured, although not crystalline.

The dependence of the 1D spectrum on lipid composition was also investigated. As displayed in Figure 3, significantly different spectra were obtained for FP23-F8 for samples made with either (a) pure DTPC or (b) LM-1 dispersions. The (a) and (b) samples were made using preparation method (1) at a 1:200 peptide:lipid mole ratio. In (a), the raw spectrum is displayed while in (b) a difference spectrum is displayed between the FP23-F8/LM-1 sample and a pure LM-1 sample. (b) is best described by a single component with fwhm line width ~ 2.7 ppm, and reflects a relatively

structured F8 residue. In (a), the spectrum is best described by two partially resolved components which likely correspond to at least two distributions of structures, each with significant population. It is unlikely that either component in (a) has a large contribution from the $\sim 20\%$ natural-abundance peptide carbonyl signal because an unlabeled FP23/DTPC sample at a 1:80 peptide:lipid ratio generated a broad carbonyl absorption which ranged from 167 to 174 ppm.

The different spectral line shapes in (a) and (b) demonstrate that there is some dependence of peptide structure on lipid composition. Although we have not yet understood the precise lipid compositional factors which cause the structural differences reflected in (a) and (b), we have observed spectra similar to (b) at a $\sim 1:100$ peptide:lipid mole ratio for samples made with LM-2 and LM-3. These mixtures differ from LM-1 only through addition of sphingomyelin, and sphingomyelin and PI, respectively. Two representative FP23-F8/LM-3 difference spectra are displayed in Figure 3(c),(d), and were obtained from 1:80 peptide:lipid ratio samples made with preparation method (1) using respectively LM-3 lipid dispersion or 100 nm diameter LM-3 vesicles. These difference spectra were obtained from subtraction between FP23-F8 and unlabeled FP23 samples and thus are nearly pure F8 signals.

The spectra from LM samples appear to be fairly independent of initial peptide concentration in the range of 12–120 μM and also independent of peptide:lipid ratio in the range of 1:200 to 1:20. For example, the samples in Figure 3(b),(c) were respectively made with 120 and 12 μM initial peptide concentrations and 1:200 and 1:80 peptide:lipid ratios. In addition, difference spectra for other labeled nuclei (e.g., V2, F11, and A15) are comparable at 1:100 and 1:20 peptide:lipid ratios (data not shown). Although the (b)–(d) spectra were made with pH 7.0 HEPES, similar spectra were also obtained when unbuffered water (pH ~ 6) was used and when 5 mM pH 5.0 acetate buffer was used.

Spectra of samples made with DTPC also had little dependence on initial peptide concentration but had some dependence on peptide:lipid ratio. For example, the two-component spectrum in Figure 3(a) is similar in appearance to one observed for a 1:133 FP23-L7F8/DTPC sample made by preparation method (2). For this latter sample, the initial peptide concentration was 1.5 mM, which is more than an order of magnitude greater than the 120 μM concentration used for sample (a). However, as displayed in Figure 2(d), a sample made with DTPC, 7.5 mM initial peptide concentration, and 1:20 peptide:lipid mole ratio gives a significantly different spectrum than that in Figure 3(a). The single-component 2(d) spectrum closely resembles the Figure 3(b–d) spectra of samples made with LM.

In addition, spectra showed little dependence on whether samples were slowly cooled during ~ 1 min while spinning in the NMR probe or were frozen in ~ 1 s by immersion of the sample rotor in liquid nitrogen. Similar spectra were also obtained after freeze/thaw cycling and after incubation of the sample at 37°C for 1.5 h (data not shown).

In summary, our 1D spectral data suggest: (1) little dependence of structural distributions on initial peptide concentration for either LM or DTPC samples; (2) little dependence of structural distributions on peptide:lipid ratio for samples made with LM; and (3) significant dependence

Table 3: Structural Correlations from Chemical Shift and 2D Exchange Analyses

residue	experimental CS (ppm)	α helical CS range (ppm) ^a	β strand CS range (ppm) ^a	CS predicted structure	2D exchange best fit ϕ, ψ
Ala-1	171.9	177.0–179.3	174.4–176.9	β strand	nd ^b
Val-2	172.2	174.0–177.6	171.8–174.2	β strand	–160°, 140°
Phe-8	170.6	174.4–176.8	169.8–174.6	β strand	–120°, 115°
Gly-10	168.4	173.4–174.8	169.6–173.0	β strand	nd
Phe-11	170.3	174.4–176.8	169.8–174.6	β strand	–165°, 140°
Ala-14	173.4	177.0–179.3	174.4–176.9	β strand	nd
Ala-15	173.2	177.0–179.3	174.4–176.9	β strand	–145°, 140°

^a Wishart et al. (84). Each range corresponds to about 90% of the residues found in that conformation. ^b Not determined.

of structural distributions on peptide:lipid ratio for samples made with DTPC. To our knowledge, the first and second observations are new information. These data strongly suggest that fusion peptide/lipid samples should be prepared with LM rather than single lipids.

1D NMR Spectral Scanning down the FP23 Backbone. Difference spectra for LM-bound FP23 peptide are displayed in Figure 4(a)–(h) and are composed of signals from labeled Ala-1, Val-2, Phe-8, Gly-10, Phe-11, Ala-14, Ala-15, and Ala-21 carbonyls, respectively. The samples were made by preparation method (1) with a peptide:lipid mole ratio of 1:100. The Val-2, Phe-8, Phe-11, Ala-15, and Ala-21 spectra are from samples made with LM-2 while the Ala-1, Gly-10, and Ala-14 spectra are from samples made with LM-3. Signals for labels between Ala-1 and Ala-15 all contained a relatively sharp feature with a line width of 2–3.5 ppm which suggests that a large population of membrane-bound peptide molecules shares a common structure at each labeled site. The approximately symmetric line shapes for Phe-8, Gly-10, Phe-11, and Ala-14 suggest that the peptide center has a high degree of structural order in a membrane environment. By contrast, the ~5 ppm line width of FP23-A21 indicates a higher degree of structural disorder at this site. Overall, these data are consistent with a model of insertion of the N-terminal and central residues of the peptide into the membrane and the C-terminus outside the membrane. In this model, there is greater structure for the residues within the membrane than outside the membrane. This is a reasonable premise because within the membrane, hydrogen bonding must be either inter- or intrapeptide, whereas outside the membrane, peptide–H₂O hydrogen bonds may be present and can allow for greater structural disorder.

Correlation of Carbonyl Chemical Shifts with Secondary Structure. Secondary structure at the different labeled carbonyl carbons in the membrane-bound fusion peptide was characterized using the known experimental correlation between secondary structure and NMR chemical shift (84). For peptide or protein carbonyl carbons, helical secondary structure generally correlates with downfield (to higher ppm) chemical shift while nonhelical structure correlates with upfield (to lower ppm) chemical shift. Table 3 lists the peak experimental shifts for different carbonyl nuclei in the more structured N-terminal and central regions of the LM-bound fusion peptide, the typical ranges of chemical shifts observed for different secondary structures for that residue type, and the assignment of the local secondary structure based on these data. All of the peak chemical shifts are most consistent with a nonhelical structure.

2D Exchange Constraints on Secondary Structure. Because chemical shifts only give a general indication of secondary

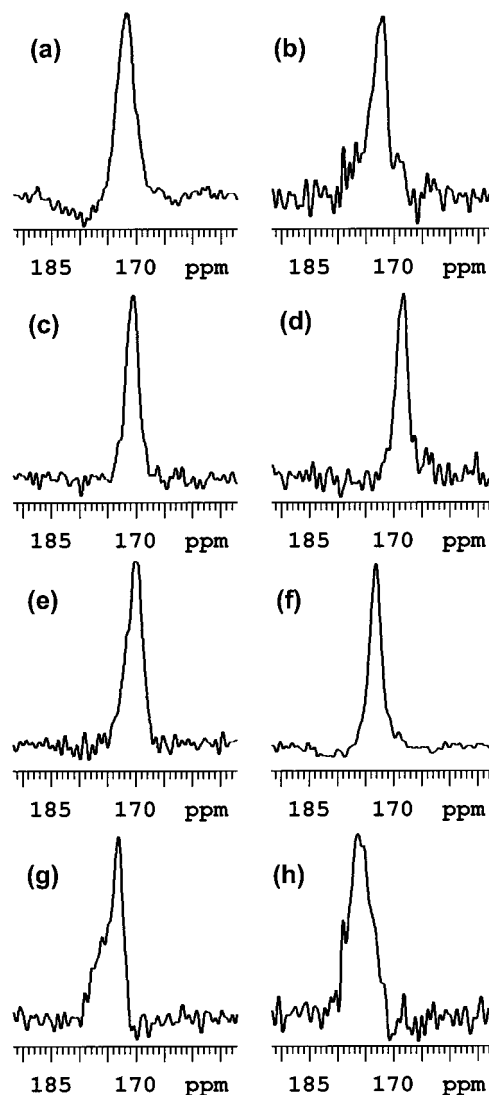


FIGURE 4: ¹³C solid-state NMR difference spectra of LM-bound (a) FP23-A1, (b) FP23-V2, (c) FP23-F8, (d) FP23-G10, (e) FP23-F11, (f) FP23-A14, (g) FP23-A15, and (h) FP23-A21. Each difference spectrum is composed of the signal from the respective labeled carbonyl nucleus. Samples were prepared by method (1) with a peptide:lipid mole ratio of 1:100. Each sample contained ~0.5 μ mol of peptide, and each spectrum is derived from 80 000–160 000 scans. Spectra were taken at –50 °C using CP/MAS and 75 kHz ¹H decoupling.

structure (helix vs strand), more precise measurements were made using 2D exchange spectroscopy on samples containing doubly carbonyl labeled peptides. These measurements typically provide dihedral angles with $\pm 20^\circ$ accuracy and can hence distinguish between various types of helical, turn, and sheet conformations. In addition, consistency between

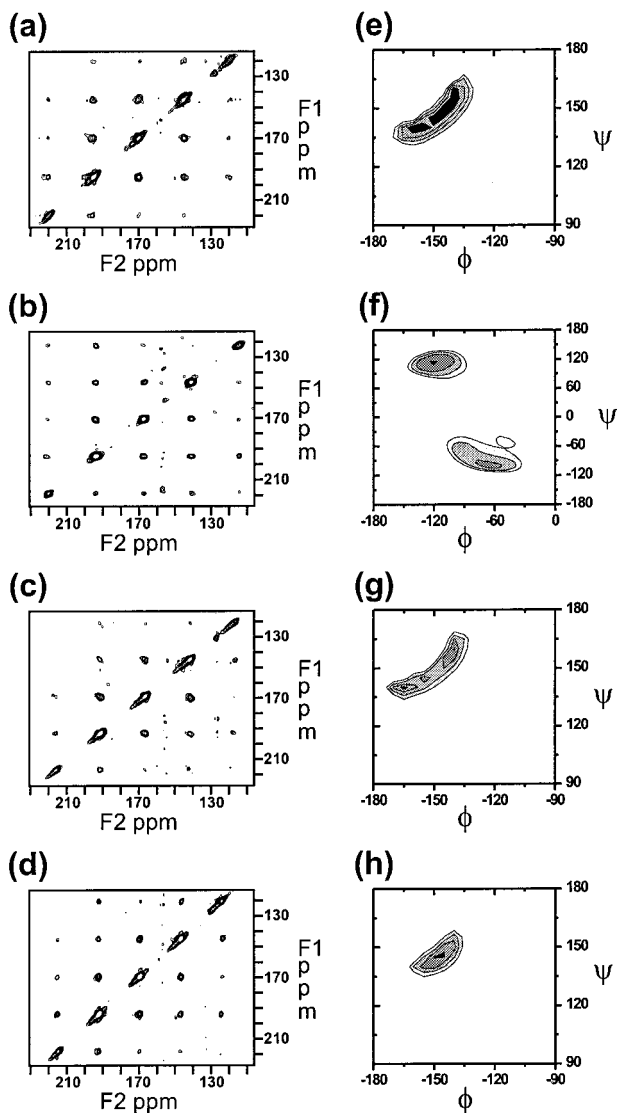


FIGURE 5: 2D ^{13}C solid-state NMR exchange spectra of (a) FP23-A1V2/LM-3, (b) FP23-L7F8/DTPC, (c) FP23-G10F11/LM-3, and (d) FP23-A14A15/LM-3. Method (1) was used to prepare samples (a), (c), and (d), and method (2) was used to prepare sample (b). The MAS frequency was 2.5 kHz, the exchange time was 500 ms, the recycle delay was 0.5 s, and 72 t_1 points were taken with an increment of 40 μs . Each spectrum represents the summation of 10–15 12 h data blocks. Secondary structure analyses for (a)–(d) are shown respectively in (e)–(h). These analyses are displayed as contour plots of the total squared deviation χ^2 (normalized to spectral noise) between the experimental off-diagonal cross-peak intensities and calculated cross-peak intensities for a grid of dihedral angles. The darkest regions represent values of χ^2 less than 6, 9, 12, and 12 for (e)–(h), respectively. Each lighter contour level represents an increase of 2 units in χ^2 . The white regions represent values of χ^2 greater than 12, 15, 18, and 18 for (e)–(h), respectively. For (e), (g), and (h), the nondisplayed dihedral angle regions of $-90^\circ < \phi < 0^\circ$ and $-180^\circ < \psi < 90^\circ$ would all be represented by white. For all residues, the data give a significantly better fit for β strand angles relative to α helical angles.

chemical shift and 2D exchange measurements provides much greater confidence in both types of measurements.

Figure 5(a–d) respectively displays 2D exchange spectra for FP23-A1V2/LM-3, FP23-L7F8/DTPC, FP23-G10F11/LM-3, and FP23-A14A15/LM-3, all made with 1:20 peptide:lipid mole ratio. The first, third, and fourth samples were prepared with method (1), and the second sample was prepared with method (2). Phosphate buffer (50 mM, pH

7.0) had been added to the FP23-L7F8/DTPC sample after initial peptide/lipid binding, but this had little effect on the 1D spectrum and presumably the membrane-bound peptide structure. The 1D line shapes of the LM-3 samples at 1:20 peptide:lipid ratio are comparable to their respective line shapes at 1:100 peptide:lipid ratio with 2–3 ppm fwhm line widths from each labeled carbonyl nucleus. The 1D line shape of the FP23-L7F8/DTPC sample (prior to phosphate addition) is displayed in Figure 2(d) with ~ 2 ppm line width from both nuclei. Thus, in all samples, it is reasonable to consider that the labeled nuclei of interest are in a well-structured region of the peptide.

The experimentally determined carbonyl CSA principal values were the following: FP23-A1V2/LM-3, 246, 180, 92 ppm; FP23-L7F8/DTPC, 241, 179, 93 ppm; FP23-G10F11/LM-3, 240, 174, 93 ppm; and FP23-A14A15/LM-3, 241, 186, 94 ppm. The experimental uncertainty in each principal value determination was typically ± 2 ppm. These principal values are comparable to those measured in rigid solids (44, 75) which indicates that large peptide backbone motions have been frozen out at the -50°C measurement temperature.

The analyses for FP23-A1V2/LM-3, FP23-L7F8/DTPC, FP23-G10F11/LM-3, and FP23-A14A15/LM-3 are displayed in Figure 5(e–h), respectively, and represent contour plots of the χ^2 difference between the experimental cross-peak intensities and the simulated intensities calculated for a grid of (ϕ, ψ) values. In the contour plots, black shading represents the lowest (best-fit) χ^2 , increasing lighter shades of gray represent increasing intervals of two units of χ^2 , and white shading represents all χ^2 greater than some value specified in the Figure 5 legend. One unit of χ^2 corresponds to about one confidence level (85). Only negative values of ϕ are displayed because the simulated cross-peak intensities for any (ϕ, ψ) are the same as those for the corresponding $(-\phi, -\psi)$. For (e), (g), and (h), the nondisplayed dihedral angle regions of $-90^\circ < \phi < 0^\circ$ and $-180^\circ < \psi < 90^\circ$ would all be represented by white. Table 3 presents the best-fit solid-state NMR (ϕ, ψ) for the Val-2, Phe-8, Phe-11, and Ala-15 residues of membrane-bound FP23. In all four cases, the best-fit values correspond to the β strand region, which is consistent with the nonhelical chemical shifts also presented in Table 3. The corresponding $(-\phi, -\psi)$ values are sterically disfavored for these non-glycine residues (80). Comparison of analyses using different NMR processing parameters (e.g., line broadening) suggests that each dihedral angle can be determined with a precision of about $\pm 20^\circ$.

DISCUSSION

The ultimate goal of research on fusion peptides is to gain insight into their role in inducing viral/host cell fusion. In this work, we provide strong evidence for the presence of an extended β strand conformation in the N-terminal and central regions of the membrane-bound peptide (cf. Table 3). The C-terminus is more disordered [cf. Figure 4(h)]. We interpret these data with a model of insertion of the N-terminal and central residues of the peptide into the membrane and the C-terminus outside the membrane. Within the membrane, there is greater peptide structure because hydrogen bonding must be either inter- or intrapeptide, whereas outside the membrane, greater conformational disorder is allowed because of the possibility of peptide–

H₂O hydrogen bonds. N-terminal membrane insertion of the fusion peptide is an important element of biological fusion models and is biophysically reasonable because of the apolar character of the N-terminal residues and the polar/charged character of some of the C-terminal residues. N-terminal membrane insertion is also consistent with other fluorescence, ESR, and NMR data on the HIV-1 fusion peptide (52, 61, 64, 68), but is not consistent with a recent neutron diffraction study on the SIV-1 fusion peptide which proposes C-terminal membrane insertion (86). The discrepancy between the HIV and SIV studies may arise from the lack of polar residues in the SIV sequence used in the neutron diffraction study.

In the β strand conformation, hydrogen bonding may be satisfied by a hairpin structure and/or by a parallel or antiparallel arrangement of peptide oligomers. One tertiary structure may be strongly preferred, or there may be a mixture of populations of tertiary structures. At this time, we do not have any data which would strongly favor or disfavor any of these tertiary structures. Although none of our 2D exchange constraints are specifically consistent with a turn motif of a hairpin structure, none of the measurements to-date have been made on any of the glycines which would likely be part of such a turn. In addition, the solid-state NMR spectra for LM samples were independent of peptide:lipid ratio over the range of 1:20 to 1:200, which might be evidence against a β sheet oligomer structure. However, in this range, it is also possible that the monomer–oligomer equilibrium always favors oligomers. This view is supported by ESR and fluorescence measurements which detected appreciable concentrations of oligomers at much lower peptide:lipid ratios, $\geq 1:800$ and $\geq 1:5000$, respectively (52, 61). Future solid-state NMR 2D exchange and internuclear distance measurements will investigate possible formation of hairpin and β sheet oligomer structures.

Greater peptide structural homogeneity was observed for the peptide/T-cell LM interaction relative to the peptide/DTPC interaction (cf. Figure 3). Although other investigators have observed dependence of overall structure on lipid type (46), our work is to our knowledge the first evidence of residue-specific variation of structural homogeneity with lipid composition. Our work strongly suggests that future fusion peptide studies should incorporate a lipid composition close to that of target T-cells. Another advantage of LM is that it appears that the bound peptide structural distributions are largely invariant over a $\sim 1:20$ – $1:200$ peptide:lipid ratio range. As displayed in Figures 2(d) and 3(a), and as observed by others (46), this ratio-independent structure is not found for other membrane compositions. The third advantage of LM is that it binds FP23 stronger than other lipid compositions (cf. Table 2).

It is useful to put our sample preparation methods and predominant β strand structure in the context of membrane fusion. Our methods rely on the insertion of the fusion peptide into the membrane from aqueous solution, which is likely the means by which the viral peptide domain inserts into the target cell membrane. Our lipid mixing results in Figure 1 also provide evidence for the fusogenic nature of the peptide under conditions comparable to those used in the preparation of solid-state NMR samples. Thus, the observed β strand conformation likely reflects at least the end-state fusogenic structure of the peptide domain.

Use of no NaCl rather than 100–150 mM NaCl concentrations is a major difference between our sample preparation methods and those of most other groups. We observed extensive peptide aggregation in solution even at moderate 20 mM NaCl concentrations. Our choice of no NaCl in the lipid preparation was guided in part by the sample preparation requirement that unbound peptide not pellet under ultracentrifugation conditions. In addition to the practical sample preparation issue, it is also important to consider the competition between aggregation and membrane binding in the presence of NaCl. With NaCl, it is unclear then whether the peptide is binding to the membrane as a monomer or as some larger oligomer or aggregates. It should be possible to add NaCl to the samples after the peptide has tightly bound to the membrane.

Our sample preparation methods and structural results are closest to those of the Nieva group, who inserted FP23 into the membrane from a predominantly aqueous solution and observed an overall β sheet structure with infrared spectroscopy (53, 54). Use of D₂O allowed them to separate buoyant vesicle-bound peptide from peptide pelleted in the 100 mM NaCl solution. Another sample preparation method in the literature involves codissolution of peptide and lipid in organic solvent, evaporation of the solvent, and then rehydration of the peptide/lipid mixture. This methodology has given mixed results with reports of both helical and β sheet conformations (46, 66). Our experience is that FP23 has much lower solubility in organic solvent than lipid. Therefore, the evaporation step likely involves sequential precipitation of the peptide and then the lipid. The general β strand structure observed in the solid-state NMR studies contrasts with the general helical structure observed in attenuated total reflectance (ATR) studies of samples prepared by direct peptide binding to liposomes (48, 51, 61, 65). This difference may have to do with the fact that the ATR samples were partially dried prior to measurement while the solid-state NMR samples were not dried. There is also a striking difference between the solid-state NMR β strand structure in LM vesicles and the α helical structure observed in SDS micelles (64). This contrast likely reflects a real difference between the equilibrium structure in micelles and in lipid bilayers. It may be difficult for a micelle to accommodate an oligomeric β strand peptide structure.

Our data clearly demonstrate that solid-state NMR will be a useful method for probing residue-specific structure of the membrane-bound HIV-1 fusion peptide. Studies are underway to investigate the fusion peptide tertiary structure, orientational distribution in the bilayer, and effects on bilayer structure and dynamics (87). In addition, comparative solid-state NMR studies on peptides with fusogenically disruptive mutations should provide insight into the structural features which are significant for fusogenic activity.

ACKNOWLEDGMENT

We acknowledge useful discussions with Mark Lemmon about ultracentrifugation. We acknowledge Robert Tycko for 2D MAS exchange simulation programs and for useful discussions about 2D MAS exchange analysis.

REFERENCES

1. Hernandez, L. D., Hoffman, L. R., Wolfsberg, T. G., and White, J. M. (1996) *Annu. Rev. Cell Dev. Biol.* 12, 627–661.

2. Blumenthal, R., and Dimitrov, D. S. (1997) in *Handbook of Physiology, Section 14: Cell Physiology* (Hoffman, J. F., and Jamieson, J. C., Eds.) pp 563–603, Oxford University Press, New York.
3. Dimitrov, D. S. (2000) *Cell* 101, 697–702.
4. Bentz, J. (2000) *Biophys. J.* 78, 886–900.
5. Wilson, I. A., Skehel, J. J., and Wiley, D. C. (1981) *Nature* 289, 366–373.
6. Bullough, P. A., Hughson, F. M., Skehel, J. J., and Wiley, D. C. (1994) *Nature* 371, 37–43.
7. Kwong, P. D., Wyatt, R., Robinson, J., Sweet, R. W., Sodroski, J., and Hendrickson, W. A. (1998) *Nature* 393, 648–659.
8. Wyatt, R., and Sodroski, J. (1998) *Science* 280, 1884–1888.
9. Gallaher, W. R. (1987) *Cell* 50, 327–328.
10. Durell, S. R., Martin, I., Ruyschaert, J. M., Shai, Y., and Blumenthal, R. (1997) *Mol. Membr. Biol.* 14, 97–112.
11. Freed, E. O., Myers, D. J., and Risser, R. (1990) *Proc. Natl. Acad. Sci. U.S.A.* 87, 4650–4654.
12. Freed, E. O., Delwart, E. L., Buchschacher, G. L., Jr., and Panganiban, A. T. (1992) *Proc. Natl. Acad. Sci. U.S.A.* 89, 70–74.
13. Schaal, H., Klein, M., Gehrmann, P., Adams, O., and Scheid, A. (1995) *J. Virol.* 69, 3308–3314.
14. Delahunty, M. D., Rhee, I., Freed, E. O., and Bonifacino, J. S. (1996) *Virology* 218, 94–102.
15. Durrer, P., Galli, C., Hoenke, S., Corti, C., Gluck, R., Vorherr, T., and Brunner, J. (1996) *J. Biol. Chem.* 271, 13417–13421.
16. Chen, J., Skehel, J. J., and Wiley, D. C. (1999) *Proc. Natl. Acad. Sci. U.S.A.* 96, 8967–8972.
17. Carr, C. M., and Kim, P. S. (1993) *Cell* 73, 823–832.
18. Kozlov, M. M., and Chernomordik, L. V. (1998) *Biophys. J.* 75, 1384–1396.
19. Bonnafous, P., and Stegmann, T. (2000) *J. Biol. Chem.* 275, 6160–6166.
20. Weissenhorn, W., Dessen, A., Harrison, S. C., Skehel, J. J., and Wiley, D. C. (1997) *Nature* 387, 426–430.
21. Chan, D. C., Fass, D., Berger, J. M., and Kim, P. S. (1997) *Cell* 89, 263–273.
22. Tan, K., Liu, J., Wang, J., Shen, S., and Lu, M. (1997) *Proc. Natl. Acad. Sci. U.S.A.* 94, 12303–12308.
23. Caffrey, M., Cai, M., Kaufman, J., Stahl, S. J., Wingfield, P. T., Covell, D. G., Gronenborn, A. M., and Clore, G. M. (1998) *EMBO J.* 17, 4572–4584.
24. Malashkevich, V. N., Chan, D. C., Chutkowski, C. T., and Kim, P. S. (1998) *Proc. Natl. Acad. Sci. U.S.A.* 95, 9134–9139.
25. Yang, Z. N., Mueser, T. C., Kaufman, J., Stahl, S. J., Wingfield, P. T., and Hyde, C. C. (1999) *J. Struct. Biol.* 126, 131–144.
26. Lu, M., Blacklow, S. C., and Kim, P. S. (1995) *Nat. Struct. Biol.* 2, 1075–1082.
27. Fass, D., Harrison, S. C., and Kim, P. S. (1996) *Nat. Struct. Biol.* 3, 465–469.
28. Kobe, B., Center, R. J., Kemp, B. E., and Pombourios, P. (1999) *Proc. Natl. Acad. Sci. U.S.A.* 96, 4319–4324.
29. Baker, K. A., Dutch, R. E., Lamb, R. A., and Jardetzky, T. S. (1999) *Mol. Cells* 3, 309–319.
30. Weissenhorn, W., Carfi, A., Lee, K. H., Skehel, J. J., and Wiley, D. C. (1998) *Mol. Cells* 2, 605–616.
31. Malashkevich, V. N., Schneider, B. J., McNally, M. L., Milhollen, M. A., Pang, J. X., and Kim, P. S. (1999) *Proc. Natl. Acad. Sci. U.S.A.* 96, 2662–2667.
32. Munoz-Barroso, I., Durell, S., Sakaguchi, K., Appella, E., and Blumenthal, R. (1998) *J. Cell Biol.* 140, 315–323.
33. Bentz, J. (2000) *Biophys. J.* 78, 227–245.
34. Griffin, R. G. (1998) *Nat. Struct. Biol.* 5 Suppl., 508–512.
35. Marassi, F. M., and Opella, S. J. (1998) *Curr. Opin. Struct. Biol.* 8, 640–648.
36. Ketchum, R. R., Hu, W., and Cross, T. A. (1993) *Science* 261, 1457–1460.
37. Kim, Y., Valentine, K., Opella, S. J., Schendel, S. L., and Cramer, W. A. (1998) *Protein Sci.* 7, 342–348.
38. Lansbury, P. T., Jr., Costa, P. R., Griffiths, J. M., Simon, E. J., Auger, M., Halverson, K. J., Kocisko, D. A., Hendsch, Z. S., Ashburn, T. T., Spencer, R. G., et al. (1995) *Nat. Struct. Biol.* 2, 990–998.
39. Benzinger, T. L., Gregory, D. M., Burkoth, T. S., Miller-Auer, H., Lynn, D. G., Botto, R. E., and Meredith, S. C. (1998) *Proc. Natl. Acad. Sci. U.S.A.* 95, 13407–13412.
40. Wang, J., Balazs, Y. S., and Thompson, L. K. (1997) *Biochemistry* 36, 1699–1703.
41. Tomita, Y., O'Connor, E. J., and McDermott, A. (1994) *J. Am. Chem. Soc.* 116, 8766–8771.
42. Studelska, D. R., McDowell, L. M., Espe, M. P., Klug, C. A., and Schaefer, J. (1997) *Biochemistry* 36, 15555–15560.
43. Jakeman, D. L., Mitchell, D. J., Shuttleworth, W. A., and Evans, J. N. (1998) *Biochemistry* 37, 12012–12019.
44. Weliky, D. P., Bennett, A. E., Zvi, A., Anglister, J., Steinbach, P. J., and Tycko, R. (1999) *Nat. Struct. Biol.* 6, 141–145.
45. Pecheur, E., Sainte-Marie, J., Bienvenue, A., and Hoekstra, D. (1999) *J. Membr. Biol.* 167, 1–17.
46. Rafalski, M., Lear, J. D., and DeGrado, W. F. (1990) *Biochemistry* 29, 7917–7922.
47. Slepishkin, V. A., Melikyan, G. B., Sidorova, M. S., Chumakov, V. M., Andreev, S. M., Manulyan, R. A., and Karamov, E. V. (1990) *Biochem. Biophys. Res. Commun.* 172, 952–957.
48. Martin, I., Defrise-Quertain, F., Decroly, E., Vandenbranden, M., Brasseur, R., and Ruyschaert, J. M. (1993) *Biochim. Biophys. Acta* 1145, 124–133.
49. Nieva, J. L., Nir, S., Muga, A., Goni, F. M., and Wilschut, J. (1994) *Biochemistry* 33, 3201–3209.
50. Mobley, P. W., Lee, H. F., Curtain, C. C., Kirkpatrick, A., Waring, A. J., and Gordon, L. M. (1995) *Biochim. Biophys. Acta* 1271, 304–314.
51. Martin, I., Schaal, H., Scheid, A., and Ruyschaert, J. M. (1996) *J. Virol.* 70, 298–304.
52. Kliger, Y., Aharoni, A., Rapaport, D., Jones, P., Blumenthal, R., and Shai, Y. (1997) *J. Biol. Chem.* 272, 13496–13505.
53. Pereira, F. B., Goni, F. M., Muga, A., and Nieva, J. L. (1997) *Biophys. J.* 73, 1977–1986.
54. Nieva, J. L., Nir, S., and Wilschut, J. (1998) *J. Liposome Res.* 8, 165–182.
55. Pritsker, M., Rucker, J., Hoffman, T. L., Doms, R. W., and Shai, Y. (1999) *Biochemistry* 38, 11359–11371.
56. Kemble, G. W., Danieli, T., and White, J. M. (1994) *Cell* 76, 383–391.
57. Shangguan, T., Alford, D., and Bentz, J. (1996) *Biochemistry* 35, 4956–4965.
58. Macosko, J. C., Kim, C. H., and Shin, Y. K. (1997) *J. Mol. Biol.* 267, 1139–1148.
59. Peuvot, J., Schanck, A., Lins, L., and Brasseur, R. (1999) *J. Theor. Biol.* 198, 173–181.
60. Slepishkin, V. A., Andreev, S. M., Sidorova, M. V., Melikyan, G. B., Grigoriev, V. B., Chumakov, V. M., Grinfeldt, A. E., Manukyan, R. A., and Karamov, E. V. (1992) *AIDS Res. Hum. Retroviruses* 8, 9–18.
61. Gordon, L. M., Curtain, C. C., Zhong, Y. C., Kirkpatrick, A., Mobley, P. W., and Waring, A. J. (1992) *Biochim. Biophys. Acta* 1139, 257–274.
62. Chang, D. K., Chien, W. J., and Cheng, S. F. (1997) *Eur. J. Biochem.* 247, 896–905.
63. Waring, A. J., Mobley, P. W., and Gordon, L. M. (1998) *Proteins: Struct., Funct., Genet., Suppl.*, 38–49.
64. Chang, D. K., Cheng, S. F., and Chien, W. J. (1997) *J. Virol.* 71, 6593–6602.
65. Mobley, P. W., Waring, A. J., Sherman, M. A., and Gordon, L. M. (1999) *Biochim. Biophys. Acta* 1418, 1–18.
66. Peisajovich, S. G., Epan, R. F., Pritsker, M., Shai, Y., and Epan, R. M. (2000) *Biochemistry* 39, 1826–1833.
67. Taylor, S. E., Desbat, B., Blaudez, D., Jacobi, S., Chi, L. F., Fuchs, H., and Schwarz, G. (2000) *Biophys. Chem.* 87, 63–72.
68. Chang, D. K., and Cheng, S. F. (1998) *J. Biomol. NMR* 12, 549–552.
69. Chang, C. D., Waki, M., Ahmad, M., Meienhofer, J., Lundell, E. O., and Haug, J. D. (1980) *Int. J. Pept. Protein Res.* 15, 59–66.

70. Lapatsanis, L., Milias, G., Froussios, K., and Kolovos, M. (1983) *Synthesis* 8, 671–673.
71. Aloia, R. C., Tian, H., and Jensen, F. C. (1993) *Proc. Natl. Acad. Sci. U.S.A.* 90, 5181–5185.
72. Hope, M. J., Bally, M. B., Webb, G., and Cullis, P. R. (1985) *Biochim. Biophys. Acta* 812, 55–65.
73. Struck, D. K., Hoekstra, D., and Pagano, R. E. (1981) *Biochemistry* 20, 4093–4099.
74. Ellens, H., Bentz, J., and Szoka, F. C. (1985) *Biochemistry* 24, 3099–3106.
75. Weliky, D. P., and Tycko, R. (1996) *J. Am. Chem. Soc.* 118, 8487–8488.
76. Tycko, R., Weliky, D. P., and Berger, A. E. (1996) *J. Chem. Phys.* 105, 7915–7930.
77. Delaglio, F., Grzesiek, S., Vuister, G. W., Zhu, G., Pfeifer, J., and Bax, A. (1995) *J. Biomol. NMR* 6, 277–293.
78. Oas, T. G., Hartzell, C. J., McMahon, T. J., Drobny, G. P., and Dahlquist, F. W. (1987) *J. Am. Chem. Soc.* 109, 5956–5962.
79. Herzfeld, J., and Berger, A. E. (1980) *J. Chem. Phys.* 73, 6021–6030.
80. Cantor, C. R., and Shimmel, P. R. (1980) *Biophysical Chemistry*, W. H. Freeman, New York.
81. Cavanaugh, J., Fairbrother, W. J., Palmer, A. G., and Skelton, N. J. (1996) *Protein NMR Spectroscopy Principles and Practice*, Academic Press, San Diego.
82. Parente, R. A., Nir, S., and Szoka, F. C., Jr. (1988) *J. Biol. Chem.* 263, 4724–4730.
83. Parente, R. A., Nir, S., and Szoka, F. C., Jr. (1990) *Biochemistry* 29, 8720–8728.
84. Wishart, D. S., Sykes, B. D., and Richards, F. M. (1991) *J. Mol. Biol.* 222, 311–333.
85. Bevington, P. R., and Robinson, D. K. (1992) *Data Reduction and Error Analysis for the Physical Sciences*, McGraw-Hill, Boston.
86. Bradshaw, J. P., Darkes, M. J., Harroun, T. A., Katsaras, J., and Eppard, R. M. (2000) *Biochemistry* 39, 6581–6585.
87. Yang, J., Parkanzky, P. D., Khunte, B. A., Canlas, C. G., Yang, R., Gabrys, C. M., and Weliky, D. P. (2001) *J. Mol. Graphics Modell.* 19, 129–135.

BI0100283